ISSN: 2319-5967
ISO 9001:2008 Certified
International Journal of Engineering Science and Innovative Technology (IJESIT)
Volume 3, Issue 1, January 2014

Static numerical simulation of oil mist particle size effects on a range of internal channel geometries of a cutting tool used in MQL strategy

Arnaud Duchosal, Roger Serra, René Leroy

Abstract*— The main goal of Minimum Quantity Lubrication was to transfer an oil mist in a cutting edge via the inner channel of a cutting tool. But machining inner channels in a tool body provided imperfections on inner channel geometries. These imperfections have an effect on oil particle size making up the oil mist and then were studied in this paper. First, numerical simulations of the oil mist in the channel were investigated by application of the Navier-Stokes and Lagrangian standard equations by integrating the standard k-ε turbulence model implemented in STAR CCM+ commercial software. This analysis showed the importance of maintaining small particle sizes and limiting imperfections which otherwise influence the performance of the micro spray and the effectiveness of lubrication. Experimental study was performed for the characterization of the oil mist in channels. The characteristics of the oil mist were defined as being particle velocities and sizes using optical laser methods and of consumption using the residual static gravimetric method. Comparison between experimental and numerical simulation results in the static validation step provided very good accuracy in terms of oil particle velocities as a function of the inlet pressure. Experimental results have shown the sputtering effect at specific configurations as predicted with efficiency in the numerical simulation.

***Index Terms*— Minimum Quantity Lubrication (MQL), multiphase flow, k-ε turbulence model, Lagrangian model, Particle size, Inner cutting tool geometry.**

I. INTRODUCTION

Minimum Quantity Lubrication (MQL) has been used extensively in various mechanical industries (automotive, aeronautic, etc). Some experimental studies have advocated the use of the MQL process and have underlined its benefits [1]-[3]. Aoyama showed results on roughness (better in MQL as dry or emulsion). He insisted on keeping small particles (Ø2µm) in oil mist transfer in the inner channel of the tool. Too large (2µm<Ø<10µm) oil particles gathered together on the wall. Too small (1µm<Ø<2µm) droplets did not stick on the cutting edge [4].

The two-phase "air + oil" mixture which makes up MQL was created either outside or inside the spindle [5]. The inner channel must be subjected to careful study. The focus of the oil mist close to the cutting edge had a significant influence on lubrication performance [6]. In grooving process, the concentration of oil mist was 28.4 times greater for a difference of distance between nozzle-cutting edges of 10mm [7]. Turning process used the same process called controlled oil-mist direction (COD). Adding specific sheets changed the outside nozzle shape and improved the efficiency of the spray. Unfortunately, this process was no longer efficient for rotating tool [8]. The machining power was considerably increased due to direction flow which was opposite to the rotating tool direction. Moreover the oil mist flow was highly subjected to the aerodynamic effects of the rotating tool. Zeilmann showed that the measured temperatures for MQL internally through the tool application in drilling process were 50% smaller than those obtained with MQL applied with an external nozzle [9].

Unfortunately, there were few articles on lubrication of milling machining via inner channels. All studies to date have focused on external MQL. Rahman showed the influence of the MQL cooling with external nozzles in drilling process [10]. Roughness and flank wear were better for MQL process than those obtained at dry or flood cutting, but at low machining conditions (speed and feed rates). Reference [2] showed the influence of the outside nozzle position for milling process. The flank wear was 33% to 42% higher for a wrong position of the outside nozzle. The study of reference [4] dealt with the influence of spindle rotation and inlet pressure on particle sizes in numerical simulation. His results showed the influence of pressure and the effect of rotation of the channel on particle size with STAR CCM+ numerical simulation software. Small particle sizes (Ø<1µm) were much less subject to the effects of rotation, and there were more small particles (about Ø1µm) than particles in the range of Ø10µm (Ratio of 1:5).

ISSN: 2319-5967
ISO 9001:2008 Certified
International Journal of Engineering Science and Innovative Technology (IJESIT)
Volume 3, Issue 1, January 2014

Computer simulation was required to operate and observe the micro lubrication phenomena for different geometry and different inlet (different pressures) and outlet conditions (machining configurations). It was even more necessary for the study of varied systems. Two-phase models developed from and / or based on the used software gave very good results. The Euler-Lagrange model was widely used for two-phase flow systems [11], [12]. This included the flow of gas bubbles in a liquid [13] or bubbles in liquid with a gas such as heat exchange in open spray tower [14] or diesel injectors [15]. Li gave an overview of the different RANS flow patterns (Reynolds-Average Navier-Stokes), LES (Large Eddy Simulation), and DNS (Direct Numerical Simulation) of the wind flows and transport of pollutant particulates in the city [16]. The Lagrangian model gave very good results for flow particles in the dispersed phase. Moreover, it enabled to take into account particle tracks and then observe and calculate their velocities [17]. Furthermore, the k-ε turbulence model was easily integrated and adapted to any type of study [18]. Study of micro-lubrication flow has taken into account a dispersed phase (oil particles) in a continuous phase (air flow). An oil mist consisted of small particles of 0.1µm<Ø<100µm provided their masses, and thus their inertia, completely ignored in the flow of the continuous phase. Interaction between particles was neglected [19]. However some parameters, such as the inlet pressure, the rotation of the spindle and the internal geometry of the channels had a considerable influence on micro-lubrication efficiency [20]. The first two parameters were easily adjusted, depending on the desired cutting conditions. The machining of the internal geometries of the channels led to imperfections which required greater attention. These imperfections affected the outside particle sizes (wall effects, impact). It affected therefore the effectiveness and had an effect on the lubrication efficiency of the cutting tools [21].

In this paper, this study presented a static numerical simulation of oil mist particle size effect on a range of internal channel geometries of a cutting tool used in MQL strategy. First, numerical simulations of the oil mist in the channel were investigated by application of the Navier-Stokes and Lagrangian standard equations by integrating the standard k-ε turbulence model implemented in a STAR CCM+ commercial software. Experimental study were performed for the characterization of the oil mist in channels, in terms of particle velocity and size using optical laser methods and of consumption using the residual static gravimetric method [22]. The channel geometry and their imperfections, the different particle sizes and their behaviors depending on the inlet pressure were taken into account. The impact of particle sizes on the fluid flow was then presented. A comparison of output velocities between experimental and numerical measurements was presented. Finally, a conclusion summarized the results obtained and discussed the effect at specific configurations in the numerical simulation.

II. GOVERNING EQUATIONS

The simulations treated in this paper were a three-dimensional steady flow which involves particles in an incompressible gaz. The Lagrangian - Eulerian methods was the approach used in simulation wherein droplets or particles were presented in a Lagrangian reference frame while the continuous phase flow field was represented in an Eulerian frame. Lagrangian method was a well-known conventional technique for tracking droplet trajectories, generally combined to a continuous flow based on Reynolds-Average-Navier-Stockes equations. However, it was possible to use other carrier flow descriptions [23]. One advantage of this formula was its robustness to solve flows with rotation. Moreover, the convergence rate was in the same order as the mesh refinement [24].

A. Assumptions

Particles were spherical. Reynolds number of the dispersion was lower than 1100. Coalescence and fragmentation of particles do not happen. Interactive forces between dispersions were ignored. Thus, particles-particles interactions were neglected. The flow field was isothermal.

B. Continuous Phase

We use equations of motion for the average properties of the fluid phase. Different forms of the averaged equations of motion for the fluid phase have been proposed in the literature [25]. Fluid motion was described by the continuity equation given by (1):

$$\frac{\partial}{\partial t}\left(\rho_f \alpha_f\right)+\frac{\partial}{\partial x_j}\left(\rho_f \alpha_f u_{fi}\right)=S_f \qquad (1)$$

Where ρ_f is the constant density of the gas, α_f is the gas volume fraction and u_f is the average velocity of the gas. The subscript S_f represents the source to gas phase due to solid -gas mass transfer. In the present work, solid-gas mass

ISSN: 2319-5967
ISO 9001:2008 Certified
International Journal of Engineering Science and Innovative Technology (IJESIT)
Volume 3, Issue 1, January 2014

transfer was not considered and therefore S_f was set to zero. The momentum equation for the fluid phase was given by (2):

$$\frac{\partial}{\partial t}\left(\rho_f \alpha_f\right)+\frac{\partial}{\partial x_j}\left(\rho_f \alpha_f u_{fi}\right)=-\frac{\partial P}{\partial x_j}+\frac{\partial}{\partial x_j}\left[\alpha_f \mu_f\left(\frac{\partial u_{fi}}{\partial x_j}+\frac{\partial u_{fj}}{\partial x_i}\right)\right] -\frac{2}{3}\left[\alpha_f \mu_f \frac{\partial u_{fm}}{\partial x_m}\right]-F+\rho_f \alpha_f g_i \quad (2)$$

Where P is the pressure in the fluid, μ_f is the viscosity of the fluid phase and F is the rate of momentum exchange per unit volume between the fluid and particle phases. The detail expression for F will be given after introducing the particle distribution function.

C. Standard k-ε turbulence model

The standard k-ε model was one of the most popular turbulence models used in Computational Fluid Dynamics (CFD). Several alternatives have been proposed to estimate the effective viscosity of the turbulent continuous phase. This model of turbulence appears to perform satisfactorily [13] and was composed of two transport equations for the turbulent kinetics k (3) and its dissipation rate ε (4) defined as follows [27]:

$$\frac{\partial}{\partial t}(\rho k)+\frac{\partial}{\partial x_j}\left(\rho u_j k\right)=\frac{\partial}{\partial x_j}\left[\left(\mu+\frac{\mu_t}{\sigma_k}\right)\frac{\partial k}{\partial x_j}\right]+\rho\left(p_k-\varepsilon\right) \quad (3)$$

$$\frac{\partial}{\partial t}(\rho\varepsilon)+\frac{\partial}{\partial x_j}\left(\rho u_j \varepsilon\right)=\frac{\partial}{\partial x_j}\left[\left(\mu+\frac{\mu_t}{\sigma_\varepsilon}\right)\frac{\partial \varepsilon}{\partial x_j}\right]+\rho\left(C_{\varepsilon 1}p_k-C_{\varepsilon 2}\varepsilon\right)\frac{\varepsilon}{k} \quad (4)$$

The turbulence kinetic energy production rate was defined as follows (5):

$$p_k=\nu_t\left(\frac{\partial u_i}{\partial x_j}+\frac{\partial u_j}{\partial x_i}\right)\frac{\partial u_i}{\partial x_j} \quad (5)$$

where $\nu_t=\frac{\mu_t}{\rho}$, and turbulence viscosity μ_t was defined by the following (6):

$$\mu_t=\rho C_\mu \frac{k^2}{\varepsilon} \quad (6)$$

The standard coefficients given in Table I, for the *k-ε* model:

Table I: Constants for the k-ε turbulence model.

C_μ	$C_{\varepsilon 1}$	$C_{\varepsilon 2}$	σ_k	σ_ε
0,09	1,44	1,92	1,0	1,3

D. Dispersed phase

Particle phase equations were given by Andrew and O'Rourke [26]. The evolution of the particle phase was governed by a Liouville equation (7) for the particle distribution function $f(x_p,u_p,\rho_p,V_p,t)$, where x_p is the particle position, u_p is the particle velocity, ρ_p is the particle mass and V_p is the particle volume:

$$\frac{\partial f}{\partial t}+\frac{\partial}{\partial x_p}\left(f u_p\right)+\frac{\partial}{\partial u_p}\left(fA\right)=0 \quad (7)$$

In this equation $A=du_p/dt$ was the particle acceleration and was given by (8):

$$A=D_p\left(u_f-u_p\right)-\frac{1}{\rho_p}\frac{\partial P}{\partial x_j}+\left(1-\frac{\rho_f}{\rho_p}\right)g-\frac{1}{\alpha_p \rho_p}\frac{\partial \tau}{\partial x_j} \quad (8)$$

ISSN: 2319-5967
ISO 9001:2008 Certified
International Journal of Engineering Science and Innovative Technology (IJESIT)
Volume 3, Issue 1, January 2014

where α_p is the particle volume fraction. Equation (8) models acceleration due to hydrodynamic drag, dynamic pressure gradient, net buoyant force and gradients in the interparticles stress τ. D_p is the drag function (9) which expression from [26] was:

$$D_p = C_d \frac{3}{8}\frac{\rho_f}{\rho_p}\frac{|u_f - u_p|}{R_p} \qquad (9)$$

Where

$$C_d = \frac{24}{\mathrm{Re}}\left(\alpha_f^{-2.65} + \frac{\mathrm{Re}^{2/3}}{6}\alpha_f^{-1.78}\right),\ \mathrm{Re} = \frac{2\rho_f |u_f - u_p| R_p}{\mu_f},\ R_p = \left(\frac{3V_p}{4\pi}\right)^{1/3}$$

Where C_d is the drag coefficient, *Re* is the Reynolds number and *Rp* the particle radius (assume spherical particles). Particle-particle collisions were modeled by an isotropic interparticle stress given by Patankar [25], as in (10):

$$\tau = \frac{P_p \alpha_p^{\beta}}{\alpha_{cp} - \alpha_p} \qquad (10)$$

Where P_p has units of pressure, α_{cp} is the particle volume fraction at close packing and β is a constant. The particle volume fraction volume α_p was related to the distribution function f, by (11):

$$\alpha_p = \iiint f V_p dV_p d\rho_p du_p \qquad (11)$$

Fluid volume fraction α_f was then given by (12):

$$\alpha_f = 1 - \alpha_p \qquad (12)$$

The interphase momentum transfer function *F* was given by (13):

$$F = \iiint f V_p \rho_p \left[D_p\left(u_f - u_p\right) - \frac{1}{\rho_p}\frac{\partial P}{\partial x_j}\right] dV_p d\rho_p du_p \qquad (13)$$

The previous Eulerian/Lagrangian formulations ignored the interparticle stress term which was model approach. It can be shown by deriving the average momentum (8) that this formulation accounts for the kinetic stress that arises from local particle velocity fluctuations about the mean velocity. Moreover as seen in the assumptions, particle-particle interactions were neglected, so the interparticle stress was set to zero.

These present approaches highlighted several important features of this formulation. Especially, the global pressure P and the particle radius R_p had significant impact on the particle behavior. Indeed, these parameters had a direct impact on acceleration particle and thus on its velocity (8).

III. NUMERICAL STUDY

On this part, numerical basic inner channels were simulated. Several channels were taken into consideration with or without imperfections. Those channels shapes represented standard canalizations in a tool body. Different parameters were taken into consideration, such as channel geometries, inlet pressure and particle sizes. Those parameters played a key role in the study of particle velocities and so on spray efficiency. Simulation was performed with the STAR CCM+ software in steady state. This software uses computational fluid dynamics to solve Navier-Stokes equations integrating the k-ε turbulence model and the Lagrange model for the continuous phase and the dispersed phase, respectively.

A. Geometric model

Numerical channels have been set on standard channel geometries from experiment. Five channels were taken into consideration with the same section of Ø6mm: straight, 45° bifurcation, 45° bifurcation with imperfection, 90° bifurcation and 90° bifurcation with imperfection channels. Fig. 1 shows the meshed cross section of the Ø6mm straight channel. The channel geometry of the experiment was made up of two parts: (i) the end of the test rig channel ("Inner spindle channel" on Fig. 1) on which (ii) models with different channel shapes ("Canalization model" on Fig. 1 below) were fixed. Inlet conditions such as inlet pressure and oil flow rate were integrated to the inlet grid of the meshed channel.

ISSN: 2319-5967
ISO 9001:2008 Certified
International Journal of Engineering Science and Innovative Technology (IJESIT)
Volume 3, Issue 1, January 2014

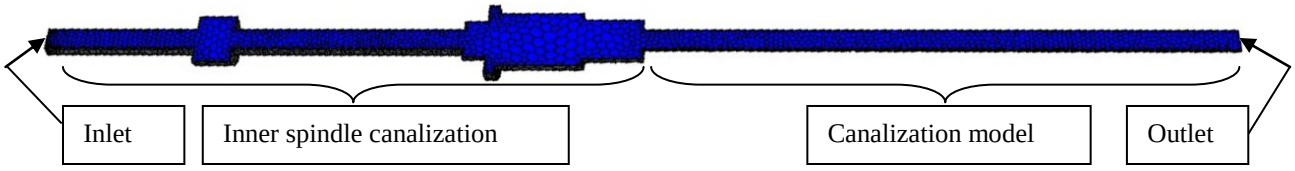

Fig. 1: Illustration of the straight Ø6mm meshing canalization model from experiment.

The half cylindrical channel was shown in sectional view in the $(\vec{x},\vec{z})$ plane along the $\vec{y}$ axis. Symmetry condition was taken into account. A 0.6 mm boundary layer was modeled to account for the edge effects. The mesh was composed of polyhedron-type elements from the STAR CCM+ software. The mesh was composed of about 40402 polyhedron cells for the Ø6mm model, 37107 cells for the 45° model, 41109 cells for the imperfect 45° model, 35920 for the 90° model and 38945 for the imperfect 90° model.

B. Boundary conditions

The working fluid used for these simulations was considered to be incompressible air at an ambient temperature of 20°C. Boundary conditions for the turbulent quantities at the model walls were specified using logarithmic wall functions.

The oil mist was governed by the Lagrangian model and rebound behavior on the channel wall was taken into consideration. The user controlled the oil density "ρ_p" and directly integrated the particle size "R_p". Because of their negligible inertia (small particle size), the dispersed phase (oil mist) has no interaction with the continuous phase (pressurized air). The model uses one-way coupling and the average consumption of 10ml.h^{-1} was chosen from the experiments.

The experimental data such as the input pressure and the oil consumption were integrated in the inlet conditions (see Fig. 1). For each channel configuration, a particle size was integrated according to the experimental data for a given oil viscosity (ν_p=80 mm^2.s^{-1}) and oil density (ρ_p=930 kg.m^{-3}). Three particle sizes were taken into consideration: Ø1µm, Ø10µm and Ø100µm. Analyses of the results for the continuous phase (pressurized air) and the dispersed phase were performed separately. The conditions for the fluid at the output were the same as the ambient air (Fig. 1).

C. Results and discussion

1) Continuous phase

Figs. 2 to 4 show the continuous phase flow velocity (pressurized air) with isolines for different channel models. In these illustrations, the inlet pressure comes from the experimental data. Numerical inlet pressures had the same values as the experimental ones. The section 4 provided different pressures for each channel geometry. These same inlet pressures with outlet velocity values were included for comparison with experiments. These comparisons contributed to the numerical model validation. For figs. 2, 3 and 4, a single value of inlet pressure of 1 bar was considered. Each channel was the same length for each model.

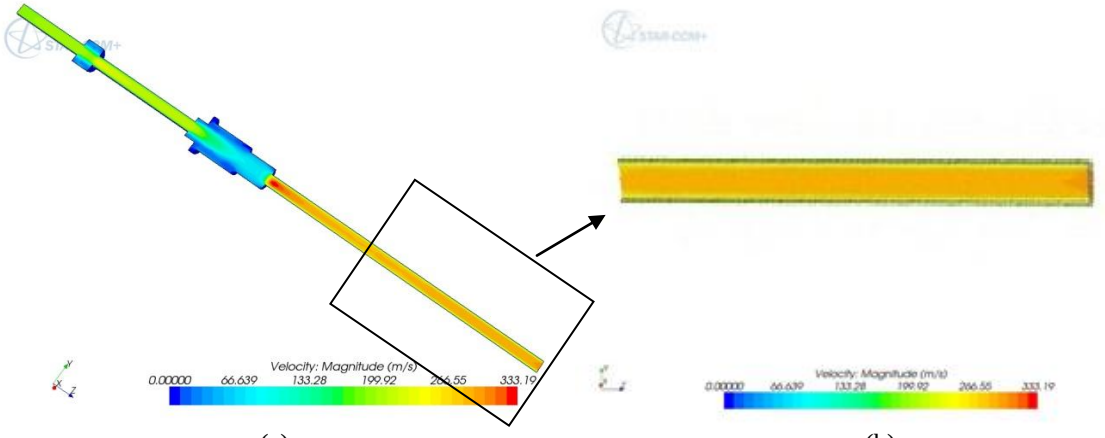

(a) (b)

Fig. 2: Illustration of the isovalues of air flow velocity a) in the full Ø6mm model, b) at the end of the canalization model, for 1 bar inlet pressure.

ISSN: 2319-5967
ISO 9001:2008 Certified
International Journal of Engineering Science and Innovative Technology (IJESIT)
Volume 3, Issue 1, January 2014

Fig. 2a shows all the numerical geometric models for the Ø6mm model. Velocities were shown in isovalues to follow them throughout the channel. At the beginning of the Ø6mm model, the maximum velocity at the diameter restriction was 333m.s^{-1}. Fig. 2b shows more precisely the outlet velocity of the Ø6mm model. The average outlet velocity at the end of the channel was about 300m.s^{-1}. It was the same for Figs. 3a and b and 4a and b which represent the isovalues for the 45°, imperfect 45°, 90° and imperfect 90° models.

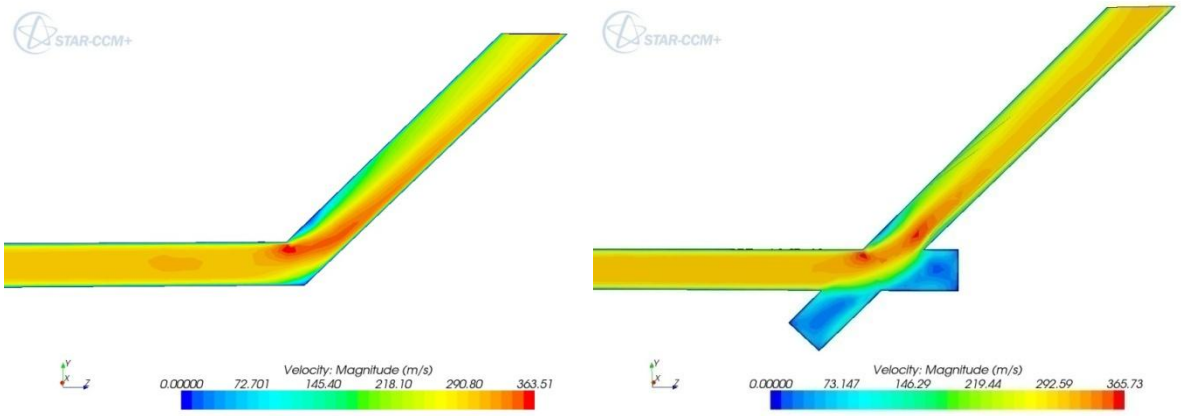

(a) (b)

Fig. 3: Illustration of the isovalues of air flow velocity at the end of a) 45°, b) imperfect 45° models, for 1 bar inlet pressure.

Fig. 3a shows the isovalues of working fluid velocity for the 45° model. The maximum velocity was located exactly in the channel bend and was about 365m.s^{-1}. Acceleration of the flow therefore occurred here, because of the geometrical features. The average velocity of the outlet channel was 275m.s^{-1}. The same phenomenon occurred in the imperfect 45° model but in two places. The first was located in the bend as above and the other right after the imperfection perpendicular to the main flow (Fig. 3b). This feature with the added imperfection can have repercussions on the behavior of "high inertia" oil particles, as discussed in the next section (Ø>10µm). The average outlet velocity was exactly the same value (275m.s^{-1}).

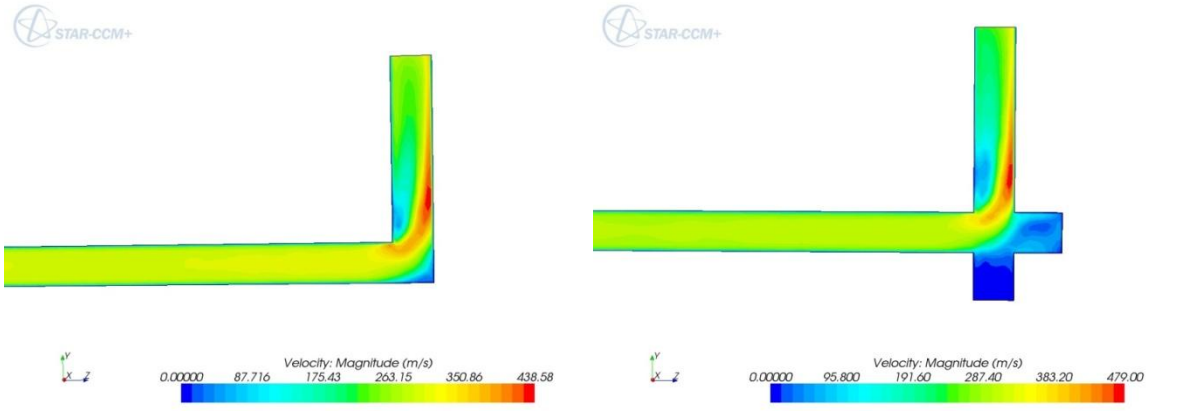

(a) (b)

Fig. 4: Illustration of the isovalues of air flow velocity at the end of a) 90°, b) imperfect 90° models, for 1 bar inlet pressure.

Figs. 4a and b show flow velocity isovalues of the working fluid for the 90° and imperfect 90° models, respectively. Because of the extreme slope of the channel (90°) the phenomenon described above was located at a slightly greater distance in the fluid flow. The same characteristic cannot be expected for higher inertia particles. The maximum velocity was observed at approximately 438m.s^{-1} and 479m.s^{-1} for the 90° and imperfect 90° models, respectively. However, the average velocities were essentially the same (275m.s^{-1} and 255m.s^{-1}).The average outlet velocity decreased with the increase in the outlet channel slope (pressure loss increased).

ISSN: 2319-5967
ISO 9001:2008 Certified
International Journal of Engineering Science and Innovative Technology (IJESIT)
Volume 3, Issue 1, January 2014

2) Dispersed phase

This section reports only the particle flows in the different models studied. The model used for the calculation was such that the particles did not affect the continuous phase flow. Oil consumption, i.e. the number of particles, did not affect the flow, or its velocity. The average consumption of 10ml.h^{-1} was used for all simulations. Moreover, the starting inlet pressure conditions were the same as those studied in the continuous phase.

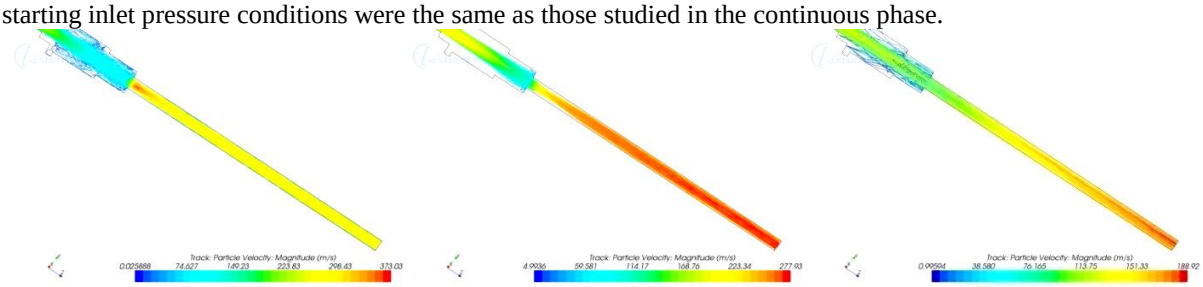

(a) (b) (c)

Fig. 5: Illustration of the dispersed phase velocity in the Ø6mm canalization model for a) Ø1µm, b) Ø10µm and c) Ø100µm particle sizes for 1 bar inlet pressure.

Figs. 5a, b and c show the dispersed phase flow for Ø1µm, Ø10µm and Ø100µm particle sizes, respectively, for the whole length of the Ø6mm channel. Fig. 5a shows Ø1µm particles for an inlet pressure of 1 bar (maximum pressure used in the study). The maximum velocity occurred in the same place as the continuous phase velocity field, just after the restriction diameter, and was about 373m.s^{-1} (333m.s^{-1} in the continuous phase).The average speed of output was maintained at 300m.s^{-1} (the same intensity as the continuous phase). For Ø10µm and Ø100µm particles, the maximum velocity was reached at the outlet channel and was about 277m.s^{-1} and 188m.s^{-1}, respectively (Figs. 5b and c). The increase in the particle sizes led to a reduction in their respective velocities. The flow model had no influence on the continuous phase flow, particles having an influence on their own behavior. Furthermore, redistribution of the particles was observed at the diameter restriction, whatever the sizes of the particles. Particles being pushed then redistributed into the main flow with the rebound effect.

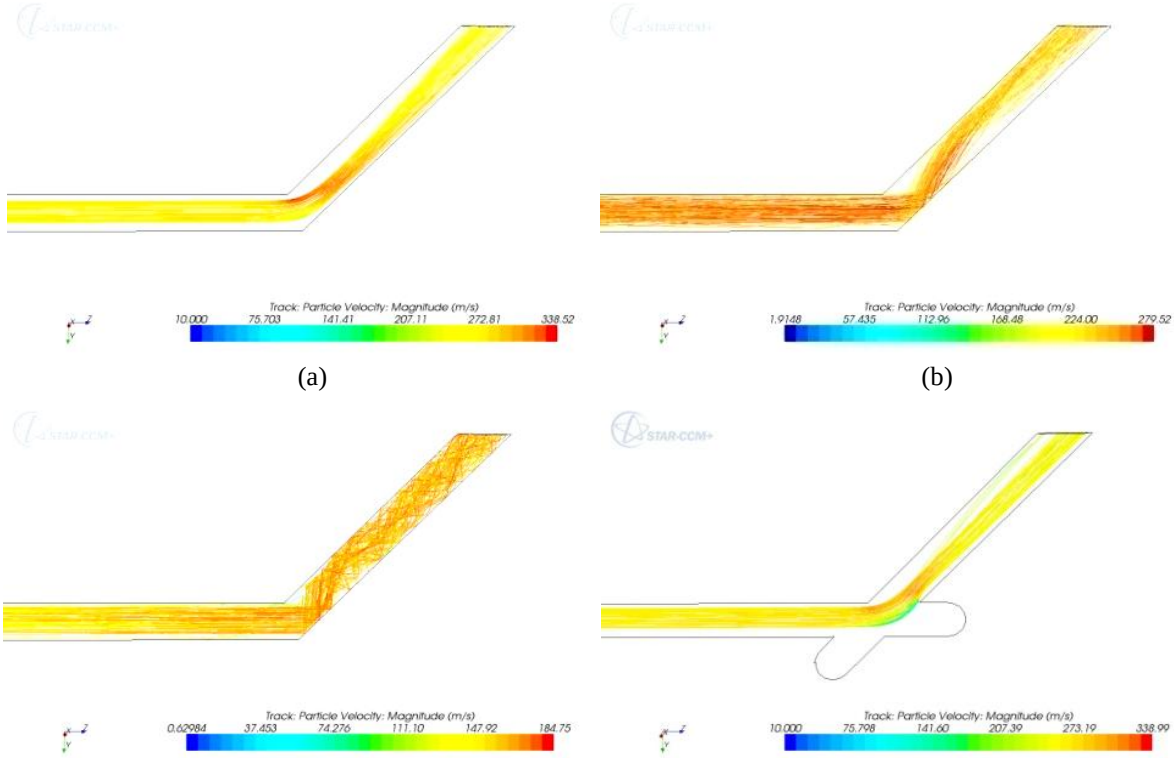

(a) (b)

(c) (d)

ISSN: 2319-5967
ISO 9001:2008 Certified
International Journal of Engineering Science and Innovative Technology (IJESIT)
Volume 3, Issue 1, January 2014

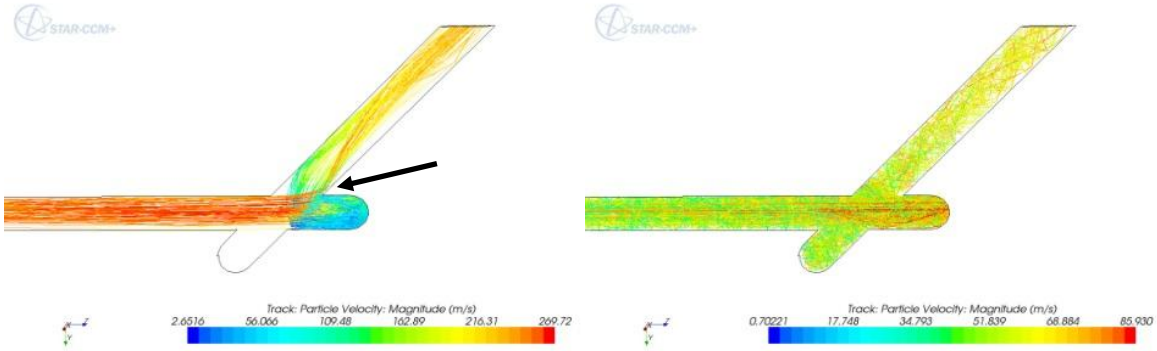

(e) (f)

Fig. 6: Illustration of the dispersed phase velocity in the 45° canalization model for a) Ø1µm, b) Ø10µm and c) Ø100µm particle sizes and in the 45° with default canalization model for d) Ø1µm, e) Ø10µm and f) Ø100µm particle sizes for 1.15 bars inlet pressure.

The flow of the particles of the 45° family channels can be seen in Fig. 6, with an inlet pressure of 1.15 bars. Figs. 6a, b and c show the flow of Ø1µm, Ø10µm and Ø100µm particles, respectively, for 45° channels. Figs. 6c, d and e represent the flow of Ø1µm, Ø10µm and Ø100µm particles, respectively, for the imperfect 45° model. For Ø1µm particles of 45° and imperfect 45° models (Figs. 6a and d, respectively), the maximum velocity was reached, and was exactly the same (338m.s^{-1}) at the bifurcation. The same velocity range was observed in the continuous phase (Figs. 3a and b). However, the average velocity was 280m.s^{-1} and 260m.s^{-1} for 45° and imperfect 45° models, respectively. An average velocity decrease was observed due to the imperfection. Although the particles underwent no visible rebound, they were attracted to the defect, causing a velocity loss (Fig. 6d) of about 7%. For Ø10 µm particles in the 45° and imperfect 45° models (Figs. 6b and e, respectively), the maximum velocities were reached just before the bifurcation and were about 279m.s^{-1} and 269m.s^{-1}, respectively. Because of the significant inertia and the rebound condition, particles collided with the channel wall (Fig. 6b) or the bottom of the defect cavity (Fig. 6e). They then followed the main flow, and their average outlet velocities were 245m.s^{-1} and 230m.s^{-1}. Regrouping occurred in the imperfect 45° model. Some particles underwent no rebound and moved in the inclination between the bifurcation corner and the imperfection hole (arrow on Fig. 6e). Finally, for Ø100µm particles in 45° and imperfect 45° models (Figs. 6c and f, respectively), the maximum velocities were reached just before the bifurcation and were about 184m.s^{-1} and 85m.s^{-1}, respectively (difference of 54%). The rebound condition for the 45° channel provided easy transfer of the particles whereas they underwent several rebounds in the bifurcation. The average velocity was about 168m.s^{-1} (Fig. 6c). Particles in the imperfect 45° model underwent severe turbulence which strongly affected the flow behavior in the dispersed phase. According to the simulation, Ø100µm particles had no chance of escaping without rebound and finished their trajectory on the channel wall (wall effect). However, the average calculated velocity of the outlet particles was 59m.s^{-1}.

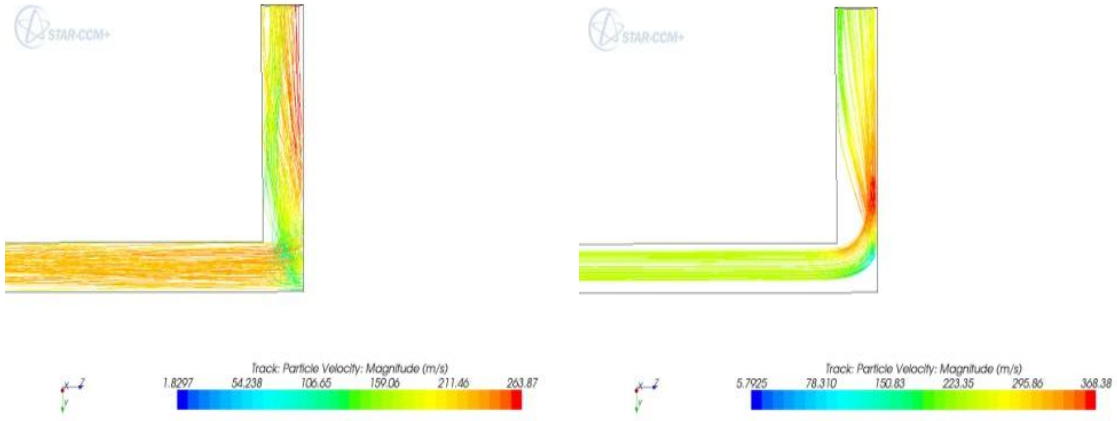

(a) (b)

ISSN: 2319-5967
ISO 9001:2008 Certified
International Journal of Engineering Science and Innovative Technology (IJESIT)
Volume 3, Issue 1, January 2014

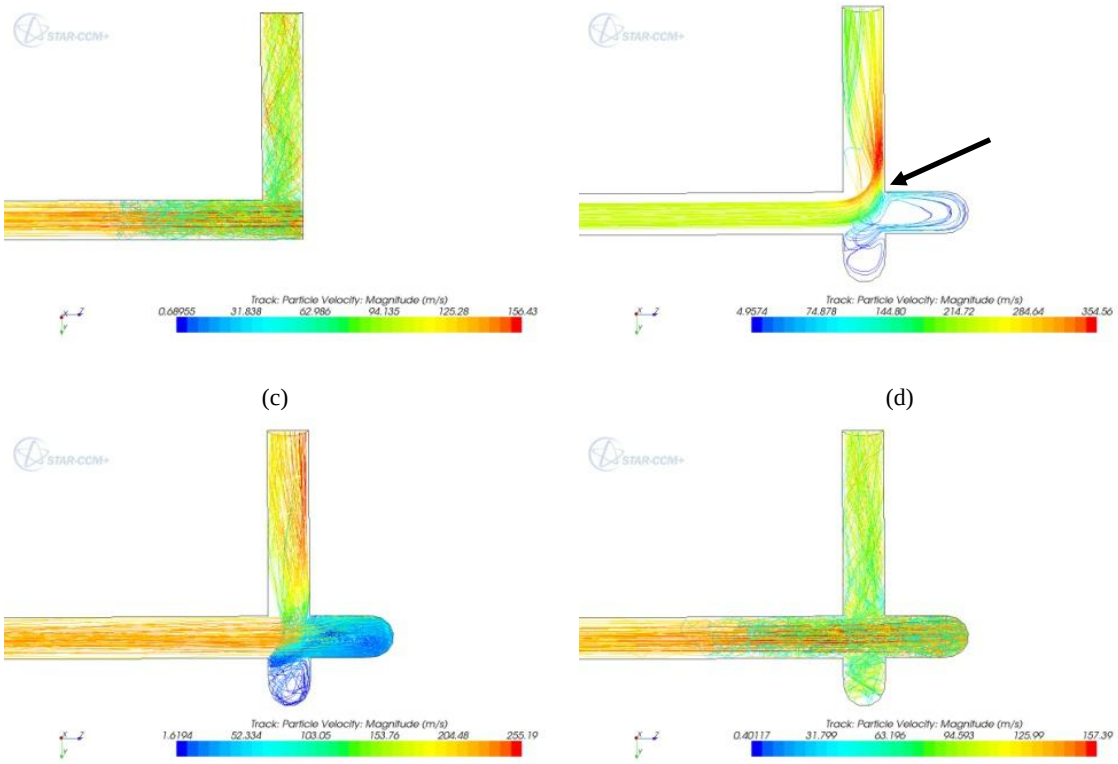

Fig. 7: Illustration of the dispersed phase velocity in the 90° canalization model for a) Ø1µm, b) Ø10µm and c) Ø100µm particle sizes and in the 90° with default canalization model for d) Ø1µm, e) Ø10µm and f) Ø100µm particle sizes for 1.35 bars inlet pressure.

Fig. 7 shows the flow of oil particles for the 90° family channels, with 1.35 bars inlet pressure. Figs. 7a, b and c illustrate the flow of Ø1µm, Ø10µm and Ø100µm particles, respectively, for the 90° channel. Figs. 7c, d and e represent the flow of Ø1µm, Ø10µm and Ø100µm particles, respectively, for the imperfect 90° model. The maximum velocity of Ø1µm particles for 90° and imperfect 90° models (Figs. 7a and d, respectively) occurred at the same place as the continuous phase (Figs. 4a and b) and reached 368m.s^{-1} and 354m.s^{-1}, respectively. The average outlet velocities were 290m.s^{-1} and 280m.s^{-1}. The imperfection in the channel had a tendency to decrease particle velocity. A large group of particles underwent no rebound effect on the wall but the remainder impacted on the right side of the channel (Fig. 7a). The same phenomenon was observed for the model with imperfection but the remainder of the particle group went to the cavity, to be re-organized in the main flow (arrow in Fig. 7d). Although the bifurcation was severe, the majority of small particles (Ø1µm) followed the flow governed by the continuous phase without rebound effect. The maximum velocity of Ø10µm particles was reached in the bifurcation at the end of the channel at 263m.s^{-1} and 255m.s^{-1} for average velocities of 260m.s^{-1} and 245m.s^{-1} (Figs. 7b and e, respectively). All particles struck in the bottom wall of the channel (Fig. 7b) or the bottom of the cavity (Fig. 7e), to be redistributed in the main flow. Finally, for Ø100µm particles in 90° and imperfect 90° models (Figs. 7c and f, respectively), maximum velocities were reached just before the bifurcation at about 156m.s^{-1}and 157m.s^{-1}, respectively. The severity of the slope, flow conditions and particle sizes (Ø100µm) resulted in strong anarchic particle behaviors. They underwent several rebounds at the bottom of the channel (Fig. 7c) or bottom of the cavity (Fig. 7f). The average outlet velocities were 135m.s^{-1} and 98m.s^{-1}, respectively.

Large particles between 10µm<Ø<100µm did not occur throughout the channel. Restrictions or bifurcation generated a rebound of particles on walls (wall effect) and reorganization in the channel in the simulation. In reality, oil was accumulated by and reorganized in the pressurized air flow. Small size particles of around Ø10µm necessarily impacted on the walls throughout the channel. The impact was greater, particularly on sudden changes in geometry shape (including bifurcations).

ISSN: 2319-5967
ISO 9001:2008 Certified
International Journal of Engineering Science and Innovative Technology (IJESIT)
Volume 3, Issue 1, January 2014

In reality, due to the wall effect, particle groups were stuck on the wall, under the boundary layer. The accumulated particles located close to the outlet exceeded the boundary layer and were suddenly removed. A large oil package was separated from the resulting in the sputtering effect at the outlet of the channel. This phenomenon occurred at the sides of the fluid outlet flow, as reported in the "Experimental validation" section (section 4).

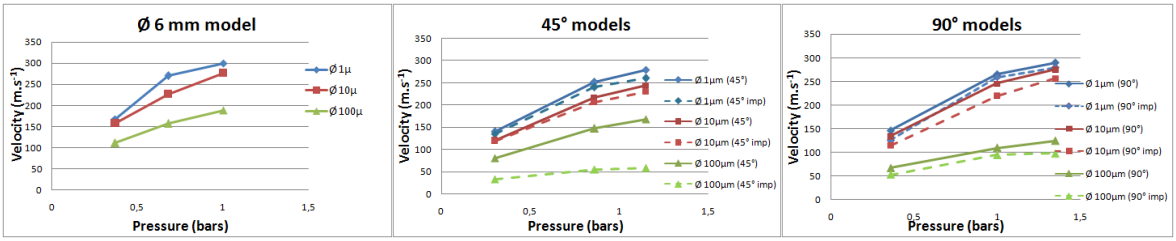

(a) (b) (c)

Fig. 8: Evolution of the outlet average velocities of the different oil mist particle sizes for the a) Ø6mm model, b) 45° models and c) 90° models in function of inlet pressure from experiment.

The velocity loss phenomenon was present for all channels with defects, for the same particle sizes and inlet pressures. Moreover, particle velocity decreased when particle size increased. Figs. 8a, b and c illustrate this velocity decreasing phenomenon for Ø6mm, 45° and 90° channels, for Ø1µm, Ø10µm and Ø100µm particles, respectively. For the Ø6mm channel (Fig. 8a), the Ø1µm particles showed the same average outlet velocity as a function of input pressure as the continuous phase, i.e.: 168m.s^{-1} for 0.37 bar, 270m.s^{-1} for 0.68 bar and 300m.s^{-1} for 1 bar. Because of their negligible inertia, particles followed the continuous phase flow velocity. The Ø10µm and Ø100µm particle velocities were lower for equivalent pressures. Particle inertia was then considered and as particle size increased, particle velocities decreased.

The 45° models in Fig. 8b showed the same trend as before. The average outlet velocities for Ø1µm particles were almost the same as those of the continuous phase for the 45° channel without defect, and were 140m.s^{-1}, 251m.s^{-1} and 280m.s^{-1} (for 0.3 bar, 0.86 bar and 1.15 bars, respectively). Velocities decreased for Ø10µm and Ø100µm particle sizes, in the same way as before. The defect in the channel significantly decreased the velocity for the same particle sizes (Ø1µm and Ø10µm). A considerable decrease in particle velocities was observed with Ø100µm particles in the imperfect model. The cumulative effects of an imperfect channel and particle sizes led to considerable velocity loss for this configuration (45°).

For 90° models in Fig. 8c, the same trend was displayed as above. The average outlet velocities for Ø1µm particles were 146m.s^{-1}, 265m.s^{-1} and 290m.s^{-1} (for 0.36 bar, 1 bar and 1.35 bars inlet pressure) in channels without imperfection. The average particle velocities were almost the same as the continuous phase velocity. Increasing particle sizes (Ø10µm and Ø100µm) decreased their own velocities. A considerable decrease in particle velocities was observed with Ø100µm particles in imperfect channels, due to the singular geometrical features. For the imperfect channels, increasing particle size substantially decreased their velocities. The Ø100µm particle velocities were considerably reduced in the 90° channel. Particle velocities were substantially reduced in the imperfect channel, as in the imperfect 45° model, for Ø100µm particle sizes.

Table II: Ø10µm and Ø100µm particle velocity losses compare with Ø1µm particle velocities, at each pressure, for Ø6mm model.

Models	Particle Sizes	Pressures (bars)		
		0.37	0.68	1
Ø6mm	Ø1µm	168m.s^{-1}	270m.s^{-1}	300m.s^{-1}
	Ø10µm	6%	16%	8%
	Ø100µm	34%	42%	38%

Tables II, III, IV summarize velocity deviations for Ø6mm, 45° and 90° models, respectively. Differences in velocity for various particles (Ø10µm and Ø100µm) were compared to Ø1µm particle velocities. Table II shows the velocity losses for Ø10µm particles (of 6% and 8% for 0.36 bar and 1 bar, respectively) compared to the particle velocity of Ø1µm. An error of 16% occurred for a pressure of 0.68 bars. Inertia was not negligible for Ø100µm particles and particle velocity was affected. A velocity loss of 34%, 42% and 38% (at 0.37 bar, 0.68 bar and 1 bar, respectively) occurred compared to Ø1µm particles.

ISSN: 2319-5967
ISO 9001:2008 Certified
International Journal of Engineering Science and Innovative Technology (IJESIT)
Volume 3, Issue 1, January 2014

Table III: Ø10µm and Ø100µm particle velocity losses compare with Ø1µm particle velocities, at each pressure, for 45° with and without imperfection models.

	Particle Sizes	Pressures (bars)		
		0.3	0.86	1.15
45°	Ø1µm	140m.s^{-1}	251m.s^{-1}	280m.s^{-1}
	Ø10µm	15%	14%	13%
	Ø100µm	43%	42%	40%
45° with imperfection	Ø1µm	135m.s^{-1}	240m.s^{-1}	260m.s^{-1}
	Ø10µm	13%	14%	12%
	Ø100µm	76%	77%	78%

Table III showed the same trend for the 45° channel. A mean velocity loss of 14% occurred for Ø10µm particles, compared to the Ø1µm particle velocities. Increase in particle diameter increased velocity loss. For Ø100µm particles, a 3 fold higher loss (average just over 41%) occurred. Adding an imperfection decreased the Ø10µm particle velocities, as for the channels without imperfection (average of 13%). Particle velocity was affected for larger particles (Ø100µm), with a loss of 77% on average (5-6 times higher).

Table IV: Ø10µm and Ø100µm particle velocity losses compare with Ø1µm particle velocities, at each pressure, for 90° with and without imperfection models.

Models	Particle Sizes	Pressures (bars)		
		0.36	1	1.35
90°	Ø1µm	146m.s^{-1}	265m.s^{-1}	290m.s^{-1}
	Ø10µm	8%	8%	11%
	Ø100µm	54%	59%	57%
90° with imperfection	Ø1µm	126m.s^{-1}	260m.s^{-1}	280m.s^{-1}
	Ø10µm	9%	16%	13%
	Ø100µm	58%	64%	65%

For the imperfect 90° model in table IV, the Ø10µm particles underwent velocity loss of 8% for 0.36 bar and 1 bar and 11% for 1.35 bars, and Ø100µm particles showed a velocity loss less than 57%, compared to the Ø1µm particle velocities. A velocity loss of about 7 times higher occurred. The Ø10µm particle velocities in the imperfect model were decreased by 9%, 16% and 13% for 0.36 bar, 1 bar and 1.35 bars, respectively. Inertia was not negligible for larger particle diameters (Ø100µm). Particle velocity was affected and an average loss of 63% was observed compared to Ø1µm particles. Losses of about 4-7 fold higher occurred.

The average particle velocities decreased considerably with channel defect for Ø100µm particle sizes. Because of their significant inertia, such particles impacted easily with channel defects. Because of the rebound conditions, particles of larger diameters may have been introduced into cavities, but completely lost their velocity. When particles were reorganized in the main flow, acceleration was less instantaneous. The average output velocity was therefore reduced. By comparison between the different particle sizes, the average velocity reduction was greater according to the increase in inlet pressure. The velocity drop was expected by equation of particle motions. Indeed, the particle acceleration equation (equ8) indirectly depended to the particle radius (R_p). The benefit of the simulation was to quantify the proportion of the velocity drop.

IV. EXPERIMENTAL VALIDATION

An experimental test rig was designed and built in order to reproduce the inner channels of the Hermle machine tools spindle. The test rig was connected to a LubriLean outside nozzle mixing device from SKF Vogel, to control inlet pressure and oil consumption.

Pressure sensors were fitted upstream (P1) and downstream (P2) of the test rig (Fig. 9) to monitor the pressure difference in the channel. Reading values were taken in P2 as references for the interpretation and validation of the results and as benchmarks for the numerical validation.

ISSN: 2319-5967
ISO 9001:2008 Certified
International Journal of Engineering Science and Innovative Technology (IJESIT)
Volume 3, Issue 1, January 2014

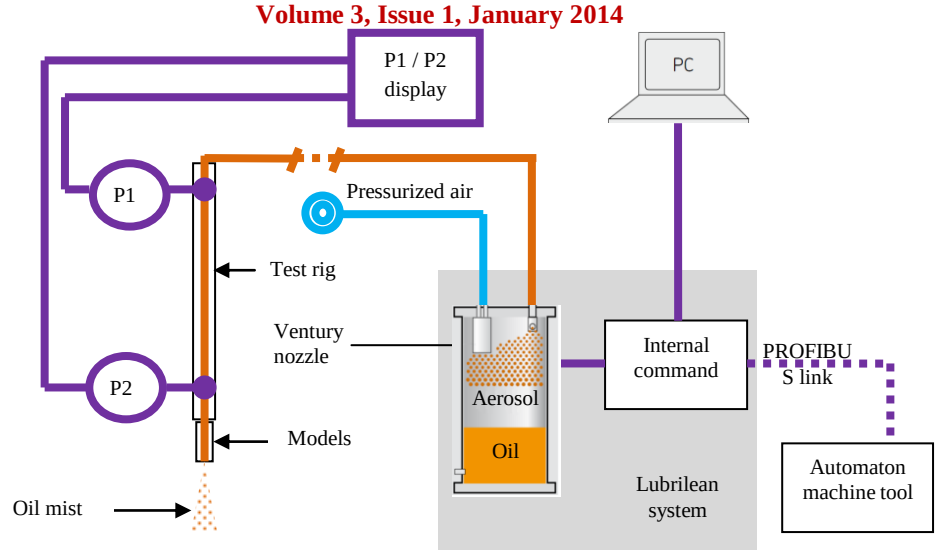

Fig. 9: The experimental test rig illustration with its two pressure gauges, along with the mist generator supported by a PC.

The test rig was designed to connect to different inner channel models that can be found on a cutting tool (Fig 10). These models simulate different ranges of geometry. Models can be found with straight Ø6mm and bifurcations of 45° and 90° channels, with or without imperfection, as seen in numerical study (section 3). These ranges of geometry show broadly what internal machine channels can generate in a tool body. The shape of the geometry creates pressure losses of ξ=0.5 for a 45° channel and ξ=1.3 for a 90° channel (with ξ: the loss coefficient). It was therefore essential to maintain a constant section to limit pressure losses.

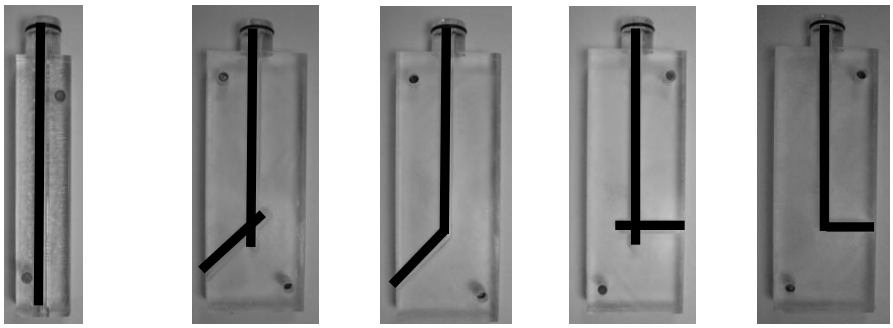

a) b) c) d) e)

Fig. 10: Illustration of the different models used a) straight Ø6mm, b) 45° with imperfection, c) 45°, d) 90° with imperfection, e) 90°.

Characterization of the oil mist was ensured by measurement of particle sizes and velocities as well as of consumption (by laser granulometry, PIV and residual gravity, respectively) for different inlet conditions and different geometry models [22].

The preliminary study involved three oils with different viscosities provided by TOTAL (Table V). Granulometry laser (particle size) and gravimetric (oil consumption) measurements showed that the oil with the highest viscosity provided the best results in terms of particle size conservation: the higher the viscosity, the less the oil accumulation on the walls and in the geometric features and the less pronounced the sputtering phenomenon.

Table V: Characteristics of the different MQL oils developed by TOTAL

	VALONA 3046	PX 5130	PX 5131
Density (15 °C) ($kg.m^{-3}$)	915	930	835
Viscosity (40 °C) ($mm^2.s^{-1}$)	46	80	28
Interfacial tension ($N.m^{-1}$)	30 - 34 $.10^{-3}$	30 - 34 $.10^{-3}$	30 - 34 $.10^{-3}$
Specific heat ($J.kg^{-1}.K^{-1}$)	1900	1900	1900
Thermal Conductivity ($W.m^{-1}.K^{-1}$)	0,14	0,14	0,14

ISSN: 2319-5967
ISO 9001:2008 Certified
International Journal of Engineering Science and Innovative Technology (IJESIT)
Volume 3, Issue 1, January 2014

It has previously been shown that the most viscous oil (PX5130) provided smaller particles for the various channels and different settings studied (0.1µm<Ø<100µm for PX5130 vs 1µm<Ø<600 µm for VALONA 3046 and PX5131). The most viscous oil PX5130 was therefore taken into consideration for this study.

Consumption was highly dependent on the generator settings and therefore determined the output air and oil flow rates. These differences in consumption were due to the solenoid valve opening considered and the additional air. Three setting configurations were taken into consideration varying from the min to the max of air and oil flow rate each. Set1 has got minimum air flow and maximum oil flow rate settings. Set2 has got maximum air flow rate and minimum oil flow rate settings. Set3 has got maximum air and oil flow rates settings (Table VI). Min air and oil flow rate settings were not considered on this study because of its not interesting results.

Table VI: Air flow rate, oil flow rate and the experimental pressure values on P1 and P2, in function of the three generator sets and different outlet geometry models.

Air Flow rate ($NL.min^{-1}$)					
	Air flow rate	Oil flow rate	Ø6mm	45°	90°
Set1	Min	Max	190	190	190
Set2	Max	Min	340	340	340
Set3	Max	Max	329	329	329
Oil flow rate ($ml.h^{-1}$)					
Set1	Min	Max	7-9	7-9	7-9
Set2	Max	Min	2-4	2-4	2-4
Set3	Max	Max	4-7	4-7	4-7
Experimental pressure values on P1 / P2					
Set1	Min	Max	0.79 / 0.37	0.79 / 0.37	0.78 / 0.36
Set2	Max	Min	1.7 / 0.68	1.87 / 0.86	1.8 / 0.79
Set3	Max	Max	2.4 / 1	2.45 / 1.15	2.5 / 1.35

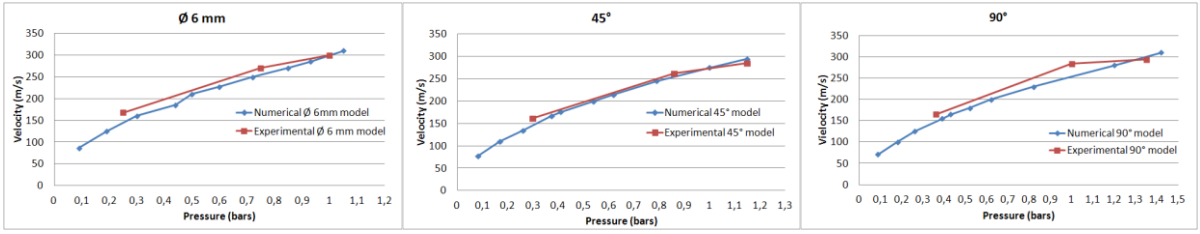

a) b) c)

Fig. 11: Experiment vs simulation correlation curves of the outlet flow average velocities for a) Ø6mm model, b) 45° model and c) 90° model.

Figs. 11a, b and c represent the correlation of average output velocities between experimental and simulation values for the Ø6mm, 45° and 90° models, respectively, over a wide pressure range (based on data from P2).For a low pressure of 0.37 bar (Fig. 11a) the outlet velocity was about $170m.s^{-1}$, the simulation provided a velocity of about $150m.s^{-1}$ (about 12%). At 0.77 bar, the experiment yielded about $270m.s^{-1}$, and the simulation $260m.s^{-1}$, or 4% error. At 1 bar, the experimental and simulation velocities were exactly the same ($300m.s^{-1}$).For the 45° model geometry (Fig. 11b) the values were similar. A difference was noted at low pressure (0.37 bar): the average experimental velocity was about $155m.s^{-1}$, and about $145m.s^{-1}$ for the simulation, i.e. a difference of 7% and values merged at 0.86 bar and 1.15 bars and $265m.s^{-1}$ and $280m.s^{-1}$. For the 90° model geometry (Fig. 11c) the average outlet velocity was about $165m.s^{-1}$, the simulation yielding about $155m.s^{-1}$, or approximately 6% error at a pressure of 0.36 bar. At 1 bar, the experiment yielded about $275m.s^{-1}$, and the simulation $250m.s^{-1}$, i.e. 9% difference. At 1.35 bars, the average velocities for the experiment and simulation merged at about $300m.s^{-1}$.

Models with defects were not shown because they consistently yielded the same velocities for the same model families. The calculated velocities were identical to those obtained by laser velocimetry, with a tendency to underestimate the velocity at low pressures. The numerical model used for the fluid flow models were validated by comparison with experiments.

During the experience, a large package of oil particles had been noticed at the outlet channels. As said before, this sputtering effect was due to the accumulation of particle groups because of the wall effects. The accumulated oil was therefore subjected to the reorganization in the flow channel. These phenomena were more pronounced in turbulent flow (set2 and set3). Oil reorganization occurs at the beginning of the channel and large particles occur

ISSN: 2319-5967
ISO 9001:2008 Certified
International Journal of Engineering Science and Innovative Technology (IJESIT)
Volume 3, Issue 1, January 2014

before the outlet. Greater dispersion was observed: the higher the oil viscosity, the less the dispersion. This phenomenon was highlighted during measurement of the particle velocities (granulometry) just after the outlet of the channel (Figs. 12, 13 and 14).

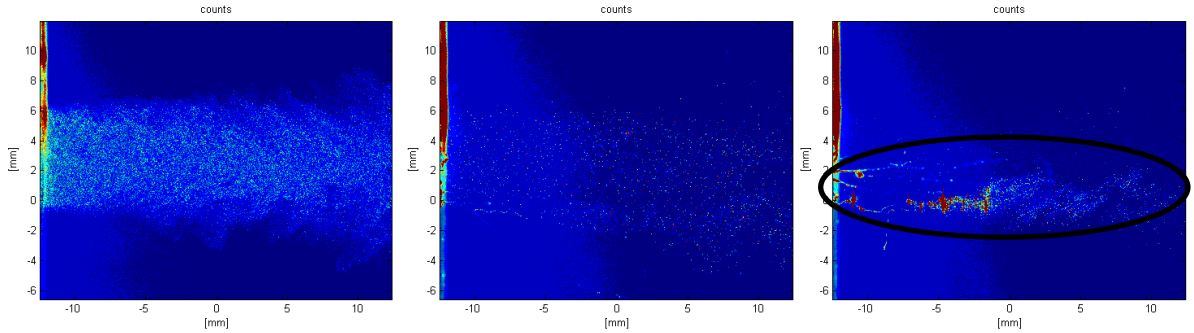

a) b) c)

Fig. 12: Illustration of the outlet oil mist just after the Ø6mm canalization (-15 mm) at a) set1, b) set2 and c) set3 generator settings and the sputtering effect (circle).

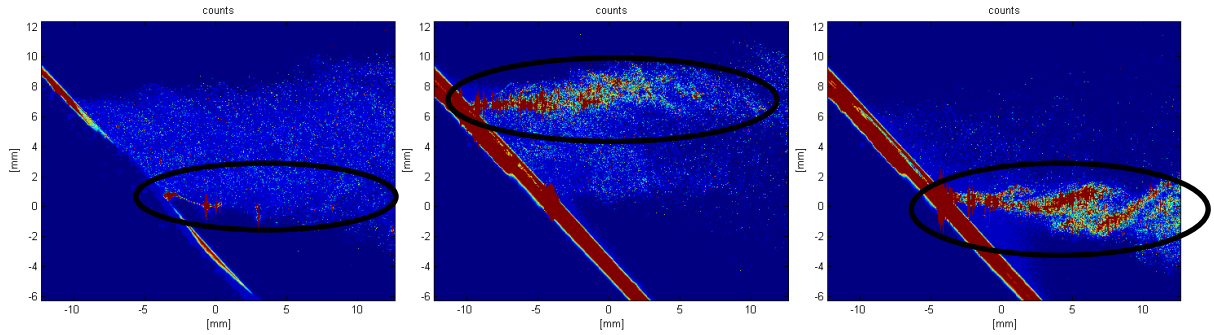

a) b) c)

Fig. 13: Illustration of the outlet oil mist just after the 45° canalization (between -5 mm and -10 mm) at a) set1, b) set2 and c) set3 generator settings and the sputtering effect (circles).

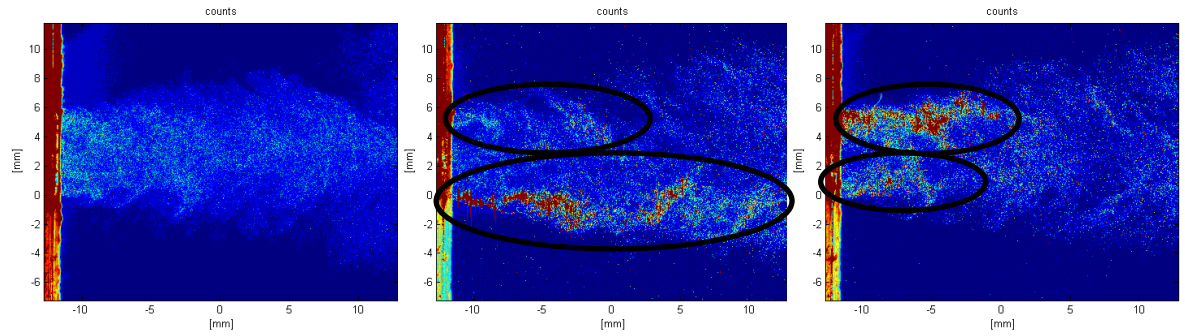

a) b) c)

Fig. 14: Illustration of the outlet oil mist just after the 90° canalization (-12 mm) at a) set1, b) set2 and c) set3 generator settings and the sputtering effect (circles).

Figs. 12, 13 and 14 show the sputtering phenomenon for Ø6mm, 45° and 90° channel models, respectively, at "*t*" time. Each Fig. shows outlet particle sizes for different oil mist generator settings at set1, set2 and set3 (a, b and c, respectively) for the chosen oil. For the Ø6 mm model, the phenomenon did not exist for still air and oil set1 and set2 setting conditions (Figs. 12a and b) but it appeared in turbulent conditions (Fig. 12c). For 45° and 90° models, the sputtering phenomenon appeared in conditions with less oil (Figs. 13b, c and 14b and c, respectively) but nevertheless turbulent (set2 and set3). These illustrations show the influence of geometric shape on the particle sizes. In still conditions (set1) large packages of particles appeared in 45° and 90° models (Figs. 13a and 14a, respectively). For the Ø6mm model, the agglomeration of oil particles was less significant (Fig 12c) compared to 45° and 90° models (Figs. 13c and 14c, respectively) for an oil mist generator setting of set3.

ISSN: 2319-5967
ISO 9001:2008 Certified
International Journal of Engineering Science and Innovative Technology (IJESIT)
Volume 3, Issue 1, January 2014

A homogenous spray was observed for set1 setting (low air pressure). Due to the small turbulence, particles from the outside nozzle mixing device kept their small dimensions by staying in the main flow. Even if particles have wall effect, the air flow rate was too low to observe sputtering effect.

Sputtering effect was observed at maximum air flow rate (set2 and set3) for all models, except for the straight canalization model at set2. The maximum air flow rate and the particular geometries (45° and 90°) increased the wall effect and the creation of large packages of particles at the outlet channel. These packages were located at the side of the outlet main flux, in the minimum velocity area.

Numerical simulations gave a good prediction of the risk of the sputtering effect. This phenomenon was determinate by the analysis of the rebound effect of the particles on the wall.

Numerical simulation highlighted the significant influence of the small particle sizes. No wall impact was noticed for small particles (except for 90° model). Large particles increased the wall effect and thus the oil accumulation. It was important to know that the wall effect was located between the nozzle mixing device and the geometric models. The use of large particles (Ø10µm and Ø100µm) simulated this approach.

V. CONCLUSION

The numerical study of the oil mist particle sizes throughout different geometric models of canalizations in MQL strategy has been presented, in this paper. The fluid motion has been simulated with the Navier-Stokes and k-ε turbulence models for the continuous phase flow (pressurized air) and the Lagrangian model was used to visualize the particle tracks in the dispersed phase. An experiment vs simulation velocity field has been compared to validate the numerical model used for this study.

Input particle sizes were modified to analyze their effects in the different geometric channels. Numerical simulation showed what happen through the channels and the following conclusions can be drawn:

- For small particles (1µm<Ø<10µm), analysis of the average outlet particle velocity showed similar velocity to the continuous phase velocity for the same channel and the same inlet pressure (small particle inertia).
- The average output velocity drop of large particles (10µm<Ø<100µm) was observed.
- The impingement of large particles against walls or in cavities (because of their non-negligible inertia) was noticed.
- Accumulated particles were reorganized in the main flow at a slower velocity but did not immediately return to their initial velocity.
- Velocity loss was observed for channels with defects (imperfections). This phenomenon was even more pronounced when the particles were larger (Inertia effect).
- Simulation has given the expected velocity drop. Geometric shape and particle sizes were taken into consideration. In general, the right responses were given faster and simpler as analytical approach.
- The presence of large particles (Ø100µm) upstream of the channel was not very probable because they were very sensitive to the diameter restrictions or to any bifurcation, because of the high inlet pressures.

In reality, oil particles were sensitive to the wall effects through the channel. Oil agglomerate was reorganized in the main fluid flow under pressure (pressurized air). Oil reorganization along the wall led to the sputtering phenomenon, which was visible on the outlet fluid flow sides.

Velocity loss with external aerodynamic conditions (machining configurations) led to less efficient lubrication. Oil particles did not reach the cutting edge. Then, small particle sizes (Ø<10µm), strong inlet conditions (P2≥1bar) and regular channel geometries were relevant for MQL effectiveness.

ACKNOWLEDGMENT

The author would like to thank Arnaud RISS from TOTAL, for his contribution to this work and for providing oils, which made this work possible. The author has a special thought for the people of CEROC for their contributions and precious advices.

REFERENCES

[1] N. R. Dhar, M. W. Islam, M. A. H. Mithu, The influence of minimum quantity of lubrication (MQL) on cutting temperature, chip and dimensional accuracy in turning AISI 1040 steel, J. Mater. Process. Technol., vol. 171, pp 93-99, 2006.

[2] L. N. Lopez de Lacalle, C. Angulo, A. Lamikiz, J. A. Sanchez, Experimental and numerical investigation on the effect of spray cutting fluids in high speed milling, J. Mater. Process. Technol., vol. 172, pp 11-15, 2006.

ISSN: 2319-5967
ISO 9001:2008 Certified
International Journal of Engineering Science and Innovative Technology (IJESIT)
Volume 3, Issue 1, January 2014

[3] P. Kalita, A. P. Malshe, S. A. Kumar, V. G. Yognath, T. Gurumurthy, Study os specific energy and friction coefficient in minimum quantity lubrication grinding using oil-based nanolubricants, J. Manuf. Process., vol. 14, pp 160-166, 2012.

[4] T. Aoyama, Development of a mixture supply system for machining with minimal quantity lubrication, CIRP Annals - Manuf Technol., vol. 51, pp 289-292, 2002.

[5] A. Attanasio, M. Gelfi, C. Giardini, C. Remino, Minimal quantity lubrication in turning: effect on tool wear, Wear, vol. 260, pp 333-338, 2006.

[6] M. Rukosuyev, C. S. Goo, M. B. G. Jun, Understanding the effects of the system parameters of an ultrasonic application system for micro-machining, J. Manuf. Process., vol. 12, pp 92-98, 2010.

[7] T. Obikawa, Y. Kamata, J. Shinozuka, High speed grooving applying MQL, Int. J. Mach. Tools Manuf., vol. 46, pp 1854-1861, 2006.

[8] T. Obikawa, Y. Kamata, Y. Asano, K. Nakayama, A. W. Otieno, Micro-litter lubrication machining of inconel 718, Int. J. Mach. Tools Manuf., vol. 48, pp 1605-1612, 2008.

[9] R. P. Zeilmann, W. L. Weingaertner, Analysis of temperature during drilling of Ti6A14V with minimal quantity of lubricant, Int. J. Mach. Tools Manuf., vol. 179, pp 124-127, 2006.

[10] M. Rahman, A. Senthil Kumar, M.U. Salam, Experimental evaluation on the effect of minimal quantities of lubricant in milling, Int. J. Mach. Tools Manuf., vol. 42, pp 539-547, 2002.

[11] A. Kitagawa, Y. Murai, F. Yamamoto, Two-way coupling of Eulerian-Lagrangian model for dispersed multiphase flows using filtering functions, Int. J. Multiphase Flow, vol. 27, pp 2129-2153, 2001.

[12] G.F. Naterer, M. Milanez, G. Venn, On the Lagrangian / Eulerian modeling of dispersed droplet inertia: Internal circulation transition, J. Colloid Interface Sci., vol. 291, pp 577-584, 2005,

[13] V.V. Buwa , D.S. Deo, V.V. Ranade, Eulerian-Lagrangian simulations of unsteady gas- liquid flows in bubble columns, Int. J. Multiphase Flow, vol. 32, pp 864-885, 2006.

[14] L. Marocco, F. Inzoli, Multiphase Euler-Lagrange CFD simulation applied to wet flue gas desulphurization technology, Int. J. Multiphase Flow, vol. 35, pp 185-194, 2009.

[15] S.V. Apte, K. Mahesh, T. Lundgren, An Eulerian-Lagrangian model to simulate two-phase/particulate flows, Center for turbulence research, Annal research briefs, pp 161-171, 2003.

[16] X. X. Li, C. H. Liu, D. Y. C. Leung, K. M. Lam, Recent progress in CFD modeling of wind field and pollutant transport in street canyons, Atmos. Environ., vol. 40, pp 5640-5658, 2006.

[17] D.G.E. Grigoriadis, S.C.Kassinos, Lagrangian particle dispersion in turbulent flow over a wall mounted obstacle, Int. J. Heat Fluid Flow, vol. 30, pp 462-470, 2009.

[18] A. Chen, E. M. Sparrow, Turbulence modeling for flow in a distribution manifold, International Journal of Heat and Mass Transfer, vol. 52, pp 1573–1581, 2009.

[19] E. Peiner, M. Balke, L. Doering, Form measurement inside fuel injector nozzle spray holes, Micro electron. Eng., vol. 86, pp 984-986, 2009.

[20] M. Emami, M. H. Sadeghi, A. A. D. Sarhan, Investigating the effects of liquid atomization and delivery of minimum quantity lubrication on the grinding process of Al_2O_3 engineering ceramics, J. Manuf. Process, vol. 15, pp 374-388, 2013.

[21] C. Nath, S. G. Kapoor, R. E. DeVor, A. K. Srivatava, J. Iverson, Design and evaluation of an atomized-based cutting fluid spray system in turning of titanium alloy, J. Manuf. Process., vol. 14, pp 452-459, 2012.

[22] A. Duchosal, R. Leroy, L. Vecellio, C. Louste, N. Ranganathan, An experimental investigation on oil mist characterization used in MQL milling process Int J Adv Manuf Technol., vol. 66, pp 1003–1014, 2013.

[23] S. Subramaniam, Lagrangian-Eulerian methods for multiphase flows, Prog. Energ. Comb. Sc., vol. 39, pp 215-245, 2013.

[24] C.M. Rhie, W.L. Chow, A numerical study of the turbulent flow past an isolated airfoil with trailing edge separation, AIAA, vol. 21, pp 1525-1532, 1983.

[25] N.A. Patankar, D.D. Joseph, Lagrangian numerical simulation of particulate flows, Int. J. Multiphase Flow, vol. 27 pp 1685-1706, 2001.

[26] M.J. Andrews, P.J. O'Rourke, The multiphase particle-in-cell (MP-PIC) method for dense particulate flows. Int. J. Multiphase Flow, vol. 22, pp 379-402, 1996.

ISSN: 2319-5967
ISO 9001:2008 Certified
International Journal of Engineering Science and Innovative Technology (IJESIT)
Volume 3, Issue 1, January 2014

[27] P.R. Spalart, Detached eddy simulation 1997–2000, Fluid Mech. Appl. Vol. 65, pp 235-237, 2004.

AUTHOR BIOGRAPHY

Arnaud Duchosal received his Master's degree in 2002 in mechanical engineering from University of Savoie, France. He has completed his PhD in june 2006 from University of Montpellier II, France. He has 4 international journal publications as main author, and 15 national and international conferences. He is currently in Tribology and Structure Dynamics Laboratory (LTDS) in Saint Etienne, France. His research interests include mechanical test analysis, machining and cutting tool, mechanical characterizations, numerical simulation processes with FE and CFD.

Roger Serra received his Master's degree in 1996 and his PhD degree in 1999 in mechanical engineering from Franche-Comté University, Besançon, France. Since 1999, he is Assistant professor at INSA Centre Val de Loire (INSA CVL), Blois, France and member of the Rheology and Mechanical Laboratory (LMR), François Rabelais University, Tours, France. He has 8 international journal publications as main authors, and 40 national and international conferences His research interests include mechanical vibration analysis and structural dynamics, experimental modal identification, structure health monitoring, machining & machining vibration's, cutting tool wear monitoring, signal processing, vibratory fatigue (HCF) and characterization mechanics.

René Leroy has completed his PhD in December 1997 from University of Toulouse, France. He has completed his D.Sc in November 2006 in Engineering Department from University of Tours, France. He has 20 international journal publication as co-author and 3 international journal publications as main author. He has participated to 39 international conferences and 32 national conferences. During his collaborations with industrials, 3 patents have been written. He is currently in Rheology and Mechanical Laboratory (LMR) in Tours, France. His research interests include mechanical analysis, machining and cutting tool, wear analysis and characterization mechanics.